

# Far-detuned mid-IR wavelength conversion at 4.05 $\mu\text{m}$ in a tellurium oxide rib waveguide pumped at 1550 nm: Design and analysis

Cite as: AIP Advances 11, 055110 (2021); doi: 10.1063/5.0049865

Submitted: 10 March 2021 • Accepted: 22 April 2021 •

Published Online: 4 May 2021



View Online



Export Citation



CrossMark

Than Singh Saini,<sup>a)</sup>  Shilpi Arora, and V. R. Supradeepa

## AFFILIATIONS

Centre for Nano Science and Engineering, Indian Institute of Science, Bengaluru 560012, Karnataka, India

<sup>a)</sup> Author to whom correspondence should be addressed: [tsinghdph@gmail.com](mailto:tsinghdph@gmail.com)

## ABSTRACT

We report the design and numerical analysis of a tellurium oxide rib waveguide pumped with femtosecond laser pulses at 1550 nm for near and mid-infrared wavelength conversion at 0.96 and 4.05  $\mu\text{m}$ , respectively. The wavelength conversion principle is based on the degenerate four-wave mixing in the designed tellurium oxide rib waveguide device. The corresponding detuning in the frequencies is as large as  $\sim 120$  THz at both sides of the pump frequency. This is the largest detuning of the frequencies obtained using a  $\text{TeO}_2$  rib waveguide via a four-wave mixing process to the best of our knowledge. Such waveguide-based light sources are required for various potential applications, including chemical sensing, absorption spectroscopy, and generation of quantum correlated photons on future nonlinear photonic integrated circuits.

© 2021 Author(s). All article content, except where otherwise noted, is licensed under a Creative Commons Attribution (CC BY) license (<http://creativecommons.org/licenses/by/4.0/>). <https://doi.org/10.1063/5.0049865>

## I. INTRODUCTION

The mid-infrared (Mid-IR) region of the electromagnetic spectrum spreading from 2–25  $\mu\text{m}$  has been considered a significant domain due to its possible numerous applications such as molecular spectroscopy and nonlinear microscopy, non-destructive testing, optical coherence tomography, and bio-photonics.<sup>1–5</sup> Most of the bio-molecules possess their absorption spectra in the mid-IR region.<sup>6</sup> Therefore, this particular region is generally known as the molecular “fingerprint region.” Furthermore, the mid-IR spectrum includes two indispensable optical windows, 3–5 and 8–13  $\mu\text{m}$ , which are transparent to the atmosphere and, therefore, very suitable for free space communication and remote sensing applications.

Undeniably, presently available mid-IR laser sources based on optical parametric oscillators (OPOs) that are being operated at wavelengths longer than 1.8  $\mu\text{m}$  are not proficient at providing the combination of the narrow linewidth and the extensive tunable range. Moreover, such OPO-based mid-IR laser sources cannot be modulated to support the innovative applications in LIDAR systems.<sup>7,8</sup> Mid-IR quantum cascade lasers (QCLs) can be tuned

broadly although the operation at room temperature still imposes the challenge for the 3–5  $\mu\text{m}$  spectral range because of the material limitations.<sup>9,10</sup> One of the favorable schemes for generating mid-IR light sources is the generation of a supercontinuum in the specialty optical fibers and waveguides.<sup>11–17</sup> Another promising scheme is the parametric wavelength conversion based on the four-wave mixing (FWM) process.<sup>18–21</sup> Signal amplification and wavelength conversion are necessary for a fully integrated wavelength division multiplexed optical network. FWM is the parametric process proficient of both converting and amplifying a signal. The frequency conversion and the broadband amplification were reported in the spectral range of 1.511–1.591  $\mu\text{m}$  by employing an all-silicon photonic chip.<sup>19</sup> Near-IR wavelength conversion at 2.388  $\mu\text{m}$  was demonstrated in a silicon waveguide device pumped at 1.589  $\mu\text{m}$  along with a probe at 1.3  $\mu\text{m}$ .<sup>20</sup> FWM has also been demonstrated on-chip in silicon wire waveguides.<sup>22,23</sup> Nonetheless, the free carrier absorption and two-photon absorption introduce nonlinear losses, which limit the efficiency of the wavelength conversion. The far-detuned parametric wavelength conversion at 2 and 3.5  $\mu\text{m}$  was demonstrated using a hybrid polymer–chalcogenide optical micro-wire pumped with a femtosecond OPO operating at

2.6  $\mu\text{m}$ .<sup>24</sup> A dispersion-engineered  $\text{As}_2\text{S}_5$  microstructured optical fiber was fabricated for parametric wavelength conversion at 4.5  $\mu\text{m}$  in an atmospheric-transparent window using an OPO providing 200 fs laser pulses at 2  $\mu\text{m}$ .<sup>25</sup> Nagasaka *et al.* demonstrated far-detuned frequency conversion over 80 THz using a 21 cm long  $\text{As}_2\text{S}_5$  chalcogenide microstructured optical fiber pumped with picosecond pulse laser pumping at  $\sim 2 \mu\text{m}$ .<sup>26</sup> In these chalcogenide fiber geometries, the optical fibers' dispersion profiles were such that they required the OPO-based pumping at the longer wavelengths (2 and 2.6  $\mu\text{m}$ ) on which the conventional compact laser sources are not available.

Silicon nitride, a CMOS compatible deposited film, does not suffer from nonlinear loss mechanisms and is still a viable material for on-chip FWM due its large Kerr response compared to glass materials.<sup>27</sup> Agha *et al.* demonstrated frequency up and down conversion between the 980 and 1550 nm wavelength regions using FWM Bragg scattering in the silicon nitride waveguides.<sup>28</sup> Kowligy *et al.* reported a dispersion-engineered nanophotonic geometry of the silicon nitride waveguide device for near-IR to mid-IR tunable light generation extending from 2.6 to 3.6  $\mu\text{m}$  on a single chip pumped by Er-fiber lasers.<sup>29</sup> However, no waveguide devices comparable to those in the mid-IR regime more than 3.6  $\mu\text{m}$  have reported to date. The main difficulty in generating mid-IR light at the wavelengths longer than 3.6  $\mu\text{m}$  is the silica substrate, which offers high absorption losses at longer wavelengths. To eliminate this difficulty, sapphire has been supposed to be the better candidate as a substrate. The sapphire as a substrate provides a number of advantages including visible-to-mid-IR optical transparency, high speed, low power, and radiation hardness.<sup>30</sup> Recently, a silicon-on-sapphire (SOS) platform was reported for the mid-IR region.<sup>31</sup> Subsequently, two types of bright quantum emitters at room temperature emitting in the orange visible spectrum, integrated in a scalable AlN-on-sapphire photonic integrated circuit platform, were reported.<sup>32</sup> It has been found that tellurium oxide ( $\text{TeO}_2$ ) is a highly promising nonlinear material for integrated photonic devices.<sup>29,33–35</sup>  $\text{TeO}_2$  is transparent within the spectrum ranging from visible to the mid-IR region with low losses of 0.1 dB/cm at 1500 nm.<sup>36–38</sup>

In this work, we have designed and numerically analyzed a  $\text{TeO}_2$  rib waveguide on the sapphire substrate for far-detuned wavelength conversion based on a four-wave mixing. The far-detuned wavelength conversion at 0.96  $\mu\text{m}$  (signal) and 4.05  $\mu\text{m}$  (idler) using a 1 cm long  $\text{TeO}_2$  rib waveguide pumped with a femtosecond laser pulse at 1.55  $\mu\text{m}$  is reported. The detuning in frequency is obtained as large as  $\sim 120$  THz. Simulated results indicate that a  $\text{TeO}_2$  rib waveguide with the dimension reported in Table I can provide mid-IR light at 4.05  $\mu\text{m}$ , which lies in the first atmospheric transparent window (i.e., 3–5  $\mu\text{m}$ ). The numerical results illustrate the  $\text{TeO}_2$  rib waveguide device's potential for far-detuned mid-IR wavelength conversion with prospective applications, including chemical sensing, absorption spectroscopy, and entangled photon pair generation.

**TABLE I.** Geometrical parameters of the designed hybrid waveguide structure.

Parameters	$h_1$ ( $\mu\text{m}$ )	$h_2$ ( $\mu\text{m}$ )	$w$ ( $\mu\text{m}$ )
Value	1	0.5	2.5

## II. DESIGN AND PROPOSED FABRICATION METHOD OF $\text{TeO}_2$ - $\text{Si}_3\text{N}_4$ HYBRID WAVEGUIDE

The schematic diagram of the  $\text{TeO}_2$  rib waveguide structure and the electric field distribution of the fundamental TE mode at 1550 nm is illustrated in Fig. 1. The waveguide structure comprises a rib waveguide deposited on the sapphire substrate. As illustrated in Fig. 1,  $h_1$ ,  $h_2$ , and  $w$  represent the height of the core, the trench depth, and the core width of the rib waveguide, respectively. From the fabrication point of view, the  $\text{TeO}_2$  film with a thickness of  $h_1$  can be deposited on a sapphire substrate by employing the radio frequency reactive sputtering technique. Finally, the rib waveguide can be patterned using electron beam lithography and reactive ion etching (RIE) techniques. The waveguide can be terminated with inverse tapers to increase coupling and make sure only the first order mode is excited. The numerical values of the geometrical parameters of the designed  $\text{TeO}_2$  rib waveguide are tabulated in Table I.

## III. RESULTS AND DISCUSSION

The wavelength-dependent refractive indices of  $\text{TeO}_2$  and sapphire materials have been estimated by employing the following Sellmeier equation [Eq. (1)], which is plotted in Fig. 2. In addition, the Sellmeier coefficients for  $\text{TeO}_2$  and sapphire materials are presented in Table II,

$$n^2 = A_0 + \sum_{n=1}^N \frac{A_n \lambda^2}{\lambda^2 - a_n^2}. \quad (1)$$

First of all, to investigate the  $\text{TeO}_2$  waveguide device, the effective mode indices of the fundamental TE mode were estimated by the full-vectorial finite element scheme. In the simulations, the fundamental TE mode has been considered. In practice, to avoid excitation of the higher order modes, one can implement an adiabatic coupling region.<sup>42</sup> The composite waveguide device's geometrical parameters were optimized to obtain appropriate zero dispersion wavelengths (ZDWs) in such a way that the waveguide is suitable for pumping at 1.55  $\mu\text{m}$ . The dispersion profile of the waveguide device plays a very important role in obeying phase-matching conditions for the FWM process to happen at a particular pump wavelength. In the process of the degenerate FWM process, two photons of an identical frequency  $\omega_p$  interact with each other via the material and annihilate to provide two new photons, i.e., signal and idler of the frequencies of  $\omega_s$  and  $\omega_i$ , respectively. In such interaction, the frequency conversion relation (energy conservation relation) is obeyed, i.e.,  $2\omega_p = \omega_s + \omega_i$ , and

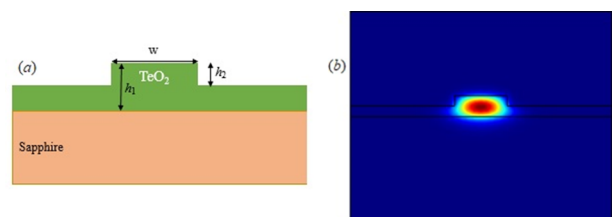


**FIG. 1.** (a) The schematic representation of the cross section of the tellurite rib waveguide deposited on the sapphire substrate. (b) The electric field distribution of the fundamental TE mode at 1550 nm confined in the core of the designed rib waveguide structure.

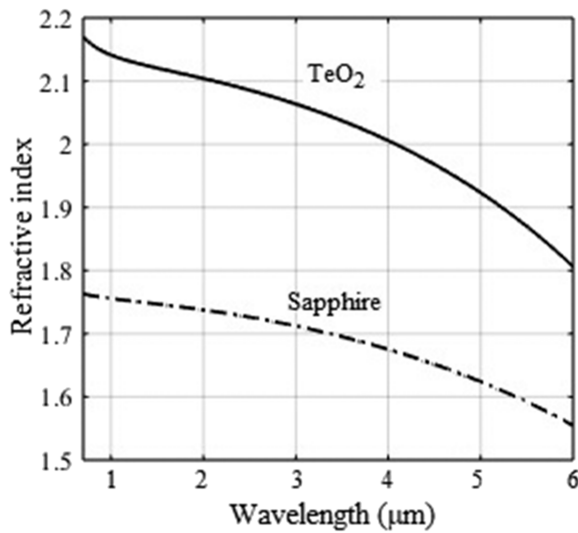


FIG. 2. The refractive indices of the TeO<sub>2</sub> and sapphire materials.

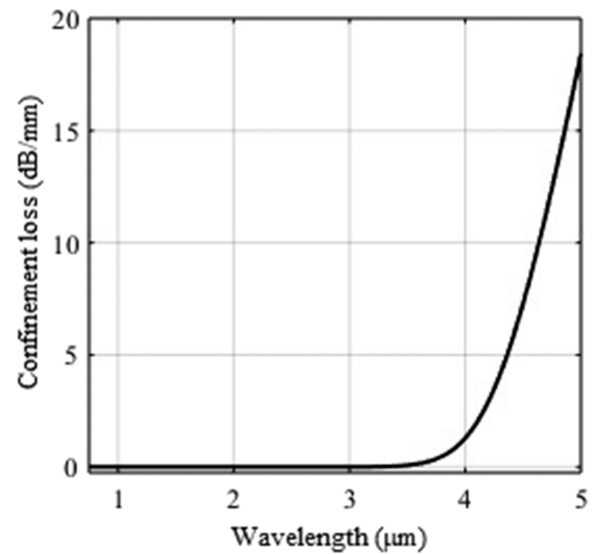


FIG. 4. The variation of the confinement loss of the propagating fundamental TE mode with wavelengths in the tellurite rib waveguide structure with  $h_1 = 1 \mu\text{m}$ ,  $h_2 = 0.5 \mu\text{m}$ , and  $w = 2.5 \mu\text{m}$ .

TABLE II. The Sellmeier coefficients of TeO<sub>2</sub> and sapphire materials.

Sellmeier coefficients	TeO <sub>2</sub> ( $\lambda$ in $\mu\text{m}$ ) <sup>39</sup>	Sapphire ( $\lambda$ in $\mu\text{m}$ ) <sup>40,41</sup>
$A_0$	3.548 303 4	1
$A_1$	0.978 372 6	1.431 349 3
$A_2$	6.651 087 9	0.650 547 13
$A_3$	...	5.341 402 1
$a_1$	0.287 522 973	0.072 663 1
$a_2$	15	0.119 324 2
$a_3$	...	18.028 251

the corresponding phase-matching condition (momentum conservation relation)  $\Delta k = 2\gamma P - (2k_p - k_s - k_i) = 0$ , where  $\Delta k$  indicates the phase mismatch between the propagation constants of the waves;  $\gamma [=2\pi \times n_2 / (\lambda \times A_{\text{eff}})]$  represents the nonlinearity coefficient (for the calculation of the nonlinear coefficient, we have used the value of the nonlinear refractive index,  $n_2 = 1.3 \times 10^{-18} \text{ m}^2/\text{W}$  for tellurite glass<sup>43</sup>);  $P$  represents the peak power of the pump; and  $k$  represents the wave vector. The pictorial representation of the energy and momentum conservation laws in the case of the degenerate FWM process is illustrated in Fig. 3.

To inspect the designed TeO<sub>2</sub> rib waveguide's performance, we considered a commercially available 180 fs laser pulse source as a

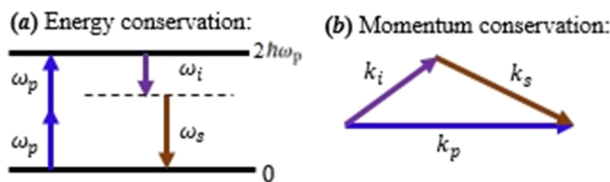


FIG. 3. Pictorial representation of (a) energy conservation and (b) momentum conservation relations.

pump with an average power of 5 mW (corresponding to the peak power of  $\sim 277 \text{ W}$ ) and the repetition rate of 100 MHz at 1550 nm. The wavelength dependence of the confinement loss of the fundamental TE mode propagating in the TeO<sub>2</sub> rib waveguide is shown in Fig. 4. We simulated the modal confinement loss ( $L$ ) of the waveguide using the imaginary part of the fundamental TE mode's effective mode index. The modal confinement loss is interrelated with the imaginary part of the effective mode index [ $\text{Im}(n_{\text{eff}})$ ] as  $L = k \times [20/\ln(10)] \times \text{Im}(n_{\text{eff}})$  [dB/m], with  $k = 2\pi/\lambda$ , where  $\lambda$  is

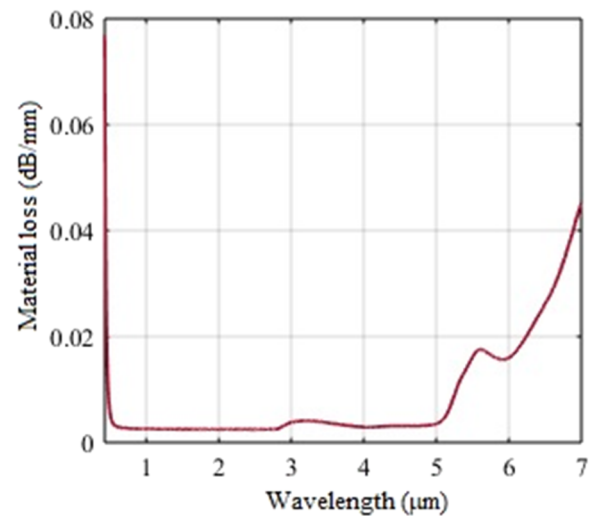


FIG. 5. The material loss of the TeO<sub>2</sub> glass.

in the unit of meter. The confinement loss of the propagating fundamental TE mode is very less for the wavelengths up to  $4 \mu\text{m}$ . The waveguide offers confinement losses of  $1.12 \times 10^{-8}$  and  $1.60 \text{ dB/mm}$  at  $1.55$  and  $4.05 \mu\text{m}$ , respectively. Figure 5 illustrates the intrinsic material loss of  $\text{TeO}_2$  glass.<sup>44</sup> As shown in Fig. 5,  $\text{TeO}_2$  glass is transparent ranging from  $0.5$  to  $5 \mu\text{m}$  with a very low material loss of  $<0.01 \text{ dB/mm}$ . The variations in the effective mode area of the fundamental TE mode with wavelengths are represented in Fig. 6. The designed  $\text{TeO}_2$  waveguide offers effective mode areas of  $1.84$  and  $11.60 \mu\text{m}^2$  for the wavelengths  $1.55$  and  $4.05 \mu\text{m}$ , respectively. The spectral variations of the nonlinear coefficient ( $\gamma$ ) for the fundamental TE mode are represented in Fig. 7. It is clear from Fig. 7 that the designed  $\text{TeO}_2$  rib waveguide offers a nonlinear coefficient as large as  $2.86$  and  $0.18 \text{ m}^{-1} \text{ W}^{-1}$  at  $1.55$  and  $4.05 \mu\text{m}$ , respectively.

The dispersion profile of the fundamental TE mode propagating in the  $\text{TeO}_2$  waveguide structure for the optimized geometrical parameters ( $t_1 = 350 \text{ nm}$ ,  $t_2 = 320 \text{ nm}$ , and  $w = 2 \mu\text{m}$ ) is depicted in Fig. 8. The designed  $\text{TeO}_2$  rib waveguide offers a dispersion value of  $61.40 \text{ ps/nm/km}$  at  $1.55 \mu\text{m}$ . Within the spectral range from  $1$  to  $4 \mu\text{m}$ , the  $\text{TeO}_2$  rib waveguide structure offers two zero-dispersion wavelengths (ZDWs) at  $1.33$  and  $2.56 \mu\text{m}$ .

The phase-matching condition for the FWM process is presented in Fig. 9. The results illustrate that, for  $1 \text{ cm}$  length of the  $\text{TeO}_2$  rib waveguide, the phase-matching condition is satisfied at  $0.96 \mu\text{m}$  (signal) and  $4.05 \mu\text{m}$  (idler) far from the pump wavelength where the value of the phase mismatch (*i.e.*,  $\Delta k$ ) is zero. The far-detuned wavelength conversion with a  $2.50 \mu\text{m}$  wavelength spacing (corresponding to the frequency shift of  $\sim 120 \text{ THz}$ ) has been accomplished toward the mid-IR region using FWM in the  $\text{TeO}_2$  rib waveguide device. Such a wavelength shift (*i.e.*, from  $1.55$  to  $4.05 \mu\text{m}$  in the mid-IR region) is the largest reported wavelength shift so far in the  $\text{TeO}_2$  rib waveguide platform. It is also important to mention

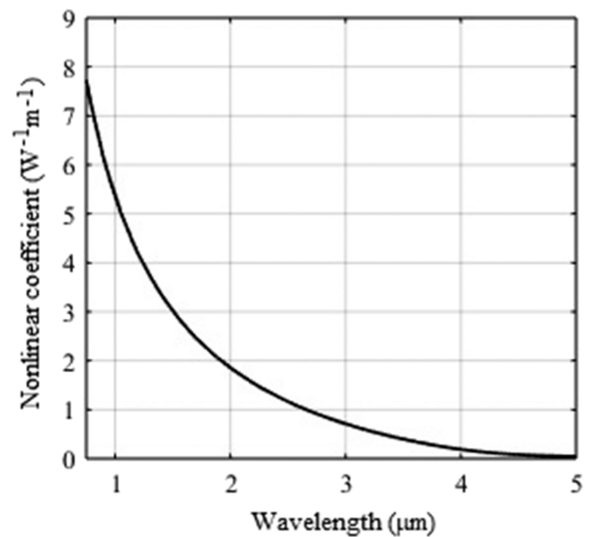


FIG. 7. The nonlinear coefficient of the propagating fundamental TE mode in the tellurite rib waveguide structure with  $h_1 = 1 \mu\text{m}$ ,  $h_2 = 0.5 \mu\text{m}$ , and  $w = 2.5 \mu\text{m}$ .

here that the phase mismatch is also zero at  $1.36$  and  $1.80 \mu\text{m}$  close to the pump wavelength. However, this is not the objective of this work. This work aims at obtaining far-detuned wavelengths toward the mid-IR region in the integrated  $\text{TeO}_2$  rib waveguide. In practice, the near detuned wavelengths can be filtered out by employing a proper optical filter at the waveguide device's output. In the degenerate FWM process, the pump wavelength is considered near the zero-dispersion wavelength of the waveguide device to avoid the longitudinal separation of the pump, signal, and idler photon pulses.

To achieve tunable features from the designed waveguide with a pump wavelength, we have analyzed the waveguide structure for the wavelength ranging from  $1.5$  to  $1.6 \mu\text{m}$ . The length of the waveguide device is considered as  $1 \text{ cm}$ . The tunable feature of

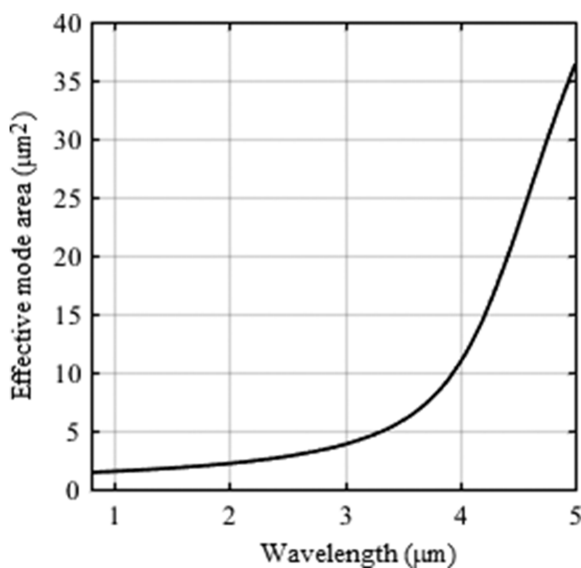


FIG. 6. The effective mode area of the propagating fundamental TE mode in the tellurite rib waveguide structure with  $h_1 = 1 \mu\text{m}$ ,  $h_2 = 0.5 \mu\text{m}$ , and  $w = 2.5 \mu\text{m}$ .

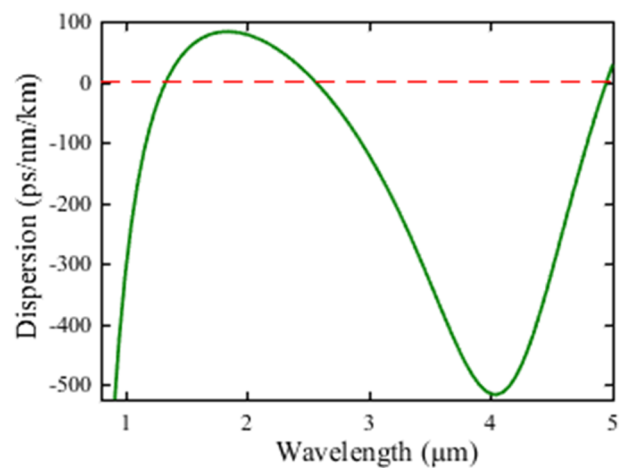
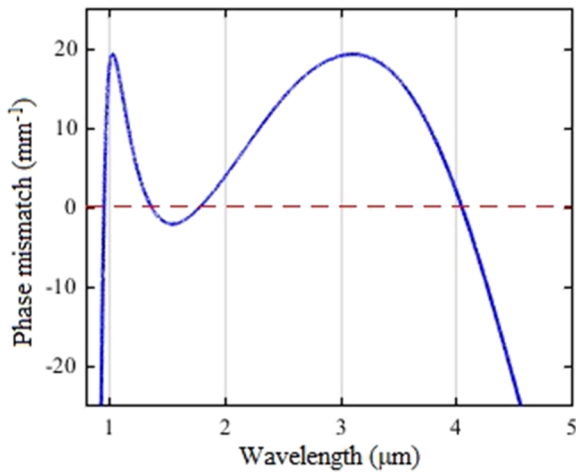


FIG. 8. The dispersion characteristic of the tellurite rib waveguide structure with  $h_1 = 1 \mu\text{m}$ ,  $h_2 = 0.5 \mu\text{m}$ , and  $w = 2.5 \mu\text{m}$ .



**FIG. 9.** The phase-mismatch ( $\Delta k$ ) for the 1 cm long composite waveguide when it is pumped by 180 fs laser pulses for an average power of 5 mW at 1550 nm.

the rib waveguide device is represented in Fig. 10. It is clear from Fig. 10 that the signal and idler waves can be tuned from 0.93 to 1.0 and 3.9–4.1  $\mu\text{m}$ , respectively, using the pump varying from 1.50 to 1.60  $\mu\text{m}$ . In this way, the signal and idler waves can be tuned by varying the pump wavelengths. This is a significant feature for photonic integrated circuits.

Finally, we performed the numerical simulations to validate the phase-matching conditions by solving the generalized nonlinear Schrodinger equation. The generalized nonlinear Schrodinger equation is given as follows:<sup>45</sup>

$$\frac{\partial \bar{A}'}{\partial z} = i\bar{\gamma}(\omega) \exp(-\hat{L}(\omega)z) \times \mathcal{F}\left\{\bar{A}(z, T) \int_{-\infty}^{\infty} R(T') |\bar{A}(z, T - T')|^2 dT'\right\}, \quad (2)$$

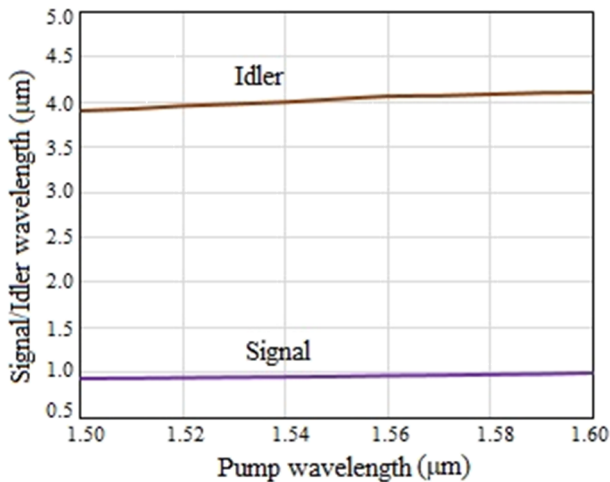


**FIG. 10.** The tunability analysis of the designed rib waveguide device when it pumped by 180 fs laser pulses of an average power of 5 mW at a pump wavelength varying from 1.5 to 1.6  $\mu\text{m}$ .

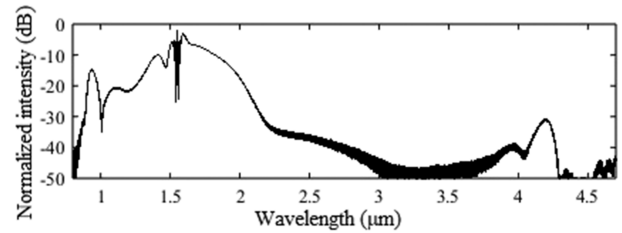


**FIG. 11.** Numerical observation of the wavelength conversion in the 1 cm long  $\text{TeO}_2$  rib waveguide pumped with 180 fs laser pulses of an average power of 5 mW at 1550 nm.

where  $\bar{A}'$  indicates the envelope of an output pulse.  $\bar{\gamma}(\omega)$  represents the frequency-dependent nonlinear coefficient.

The relation can simulate the Raman response function,

$$R(t) = (1 - f_R)\delta(T) + f_R \frac{\tau_1^2 + \tau_2^2}{\tau_1 \tau_2^2} \exp\left(-\frac{T}{\tau_2}\right) \sin\left(\frac{T}{\tau_1}\right) H(T), \quad (3)$$

where  $f_R$  represents the Raman response contribution.  $\tau_1$  is the Raman period,  $\tau_2$  is the damping time, and  $H(T)$  indicates the Heaviside step function [i.e.,  $H(T) = 0$  if  $T < 0$  and  $H(T) = 1$  if  $T > 0$ ]. For  $\text{TeO}_2$  glass, the fractional Raman contribution  $f_R = 0.064$ , Raman period  $\tau_1 = 7.4413$  fs, and lifetime  $\tau_2 = 46.932$  fs were used in the calculations.<sup>46</sup> The total loss spectrum of the  $\text{TeO}_2$  rib waveguide was estimated by adding up the confinement loss of the  $\text{TeO}_2$  rib waveguide and the intrinsic material loss spectrum of the  $\text{TeO}_2$  glass.

Figures 11 and 12 illustrate the simulated spectrum for a 1 cm long  $\text{TeO}_2$  rib waveguide pumped with 180 fs laser pulses of an average power of 5 mW at 1550 nm. As shown in Fig. 11, the signal and idler waves were obtained at the wavelengths of  $\sim 0.94 \mu\text{m}$  (slightly less than  $0.96 \mu\text{m}$ ) and  $\sim 4.15 \mu\text{m}$  (somewhat more than  $4.05 \mu\text{m}$ ), respectively. The obtained results demonstrate good agreement between FWM phase-matched wavelengths and the signal and idler wavelengths obtained by solving the Schrodinger wave equation. Figure 12 shows that the obtained frequency detuning is as large as  $\sim 120$  THz on either side of the pump frequency. This is the largest detuning of the frequencies obtained using a  $\text{TeO}_2$  rib waveguide platform via the FWM process to the best of our knowledge. The reported waveguide structure can be used to generate far-detuned wavelengths at  $\sim 0.96$  and  $\sim 4.05 \mu\text{m}$  using ultrafast laser pumping

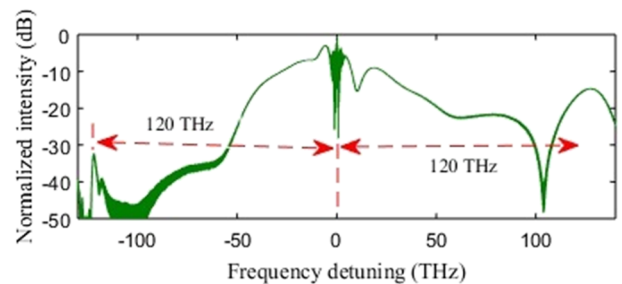


**FIG. 12.** The frequency detuning obtained in a 1 cm long  $\text{TeO}_2$  rib waveguide pumped with 180 fs laser pulses of an average power of 5 mW at 1550 nm.

at 1.55  $\mu\text{m}$ . Such nonlinear rib waveguide devices generating light at 0.96 and 4.05  $\mu\text{m}$  hold significant potential to multiply the integrated circuits' functionality for the applications in a wide range of mid-IR nonlinear integrated photonic devices.

#### IV. CONCLUSION

In summary, we have designed and numerically analyzed an integrated  $\text{TeO}_2$  rib waveguide structure on the sapphire substrate for mid-IR wavelength generation at 4.05  $\mu\text{m}$  using degenerate FWM. The wavelength of the generated idler wave lies in one of the atmospheric transparent windows (i.e., 3–5  $\mu\text{m}$ ) in the mid-IR region. The obtained results demonstrate that using a 1 cm long  $\text{TeO}_2$  rib waveguide pumped with ultrafast laser pulses at 1.55  $\mu\text{m}$ , one can achieve far-detuned wavelength conversion at 0.96  $\mu\text{m}$  (signal) and 4.05  $\mu\text{m}$  (idler) via the degenerate FWM process. The obtained signal and idler frequencies are detuned by  $\sim 120$  THz from the pump frequency. Such nonlinear waveguide devices generating light at 0.96 and 4.05  $\mu\text{m}$  hold significant potential to multiply the integrated circuits' functionality. The result shows the potential of the  $\text{TeO}_2$  rib waveguide for far-detuned mid-IR wavelength conversion with prospective applications, including chemical sensing, absorption spectroscopy, and entangled photon pair generation.

#### ACKNOWLEDGMENTS

T.S.S. acknowledges the research support from the Indian Institute of Science under the C.V. Raman Postdoctoral Fellowship scheme.

#### DATA AVAILABILITY

The data that support the findings of this study are available from the corresponding author upon reasonable request.

#### REFERENCES

- A. Labrüyère, A. Tonello, V. Couderc, G. Huss, and P. Leproux, "Compact supercontinuum sources and their biomedical applications," *Opt. Fiber Technol.* **18**, 375–378 (2012).
- R. Su, M. Kirillin, E. W. Chang, E. Sergeeva, S. H. Yun, and L. Mattsson, "Perspectives of mid-infrared optical coherence tomography for inspection and micrometrology of industrial ceramics," *Opt. Express* **22**, 15804–15819 (2014).
- F. C. Cruz *et al.*, "Mid infrared optical frequency combs based on difference frequency generation for molecular spectroscopy," *Opt. Express* **23**, 26814–26824 (2015).
- J. Nallala, G. R. Lloyd, N. Shepherd, and N. Stone, "High-resolution FTIR imaging of colon tissues for elucidation of individual cellular and histopathological features," *Analyst* **141**, 630–639 (2016).
- M. Verdonck *et al.*, "Characterization of human breast cancer tissues by infrared imaging," *Analyst* **141**, 606–619 (2016).
- A. Schliesser, N. Picqué, and T. W. Hänsch, "Mid-infrared frequency combs," *Nat. Photonics* **6**, 440–449 (2012).
- M. Bashkansky, H. R. Burris, E. E. Funk, R. Mahon, and C. I. Moore, "RF phase-coded random-modulation LIDAR," *Opt. Commun.* **231**, 93–98 (2004).
- S. Kameyama, M. Imaki, Y. Hirano, S. Ueno, S. Kawakami, D. Sakaizawa, and M. Nakajima, "Development of 1.6  $\mu\text{m}$  continuous-wave modulation hard target differential absorption LIDAR system for  $\text{CO}_2$  sensing," *Opt. Lett.* **34**, 1513–1515 (2009).
- G. Wysocki, R. Lewicki, R. F. Curl, F. K. Tittel, L. Diehl, F. Capasso, M. Troccoli, G. Hoffer, D. Bour, S. Corzine, R. Maulini, M. Giovannini, and J. Faist, "Widely

tunable mode-hop free external cavity quantum cascade lasers for high resolution spectroscopy and chemical sensing," *Appl. Phys. B* **92**, 305–311 (2008).

- O. Cathabard, R. Teissier, J. Devenson, and A. N. Baranov, "InAs-based distributed feedback quantum cascade lasers," *Electron. Lett.* **45**, 1028–1030 (2009).
- T. S. Saini, U. K. Tiwari, and R. K. Sinha, "Rib waveguide in Ga-Sb-S chalco-genide glass for on-chip mid-IR supercontinuum sources: Design and analysis," *J. Appl. Phys.* **122**, 053104 (2017).
- T. S. Saini, N. P. T. Hoa, L. Xing, T. H. Tuan, T. Suzuki, and Y. Ohishi, "Chalcogenide W-type co-axial optical fiber for broadband highly coherent mid-IR supercontinuum generation," *J. Appl. Phys.* **124**, 213101 (2018).
- C. R. Petersen, U. Möller, I. Kubat, B. Zhou, S. Dupont, J. Ramsay, T. Benson, S. Sujecki, N. Abdel-Moneim, Z. Tang, D. Furniss, A. Seddon, and O. Bang, "Mid-infrared supercontinuum covering the 1.4–13.3  $\mu\text{m}$  molecular fingerprint region using ultra-high NA chalcogenide step-index fibre," *Nat. Photonics* **8**, 830–834 (2014).
- T. S. Saini, A. Kumar, and R. K. Sinha, "Broadband mid-infrared supercontinuum spectra spanning 2–15  $\mu\text{m}$  using  $\text{As}_2\text{Se}_3$  chalcogenide glass triangular-core graded-index photonic crystal fiber," *J. Lightwave Technol.* **33**(18), 3914–3920 (2015).
- T. S. Saini, U. K. Tiwari, and R. K. Sinha, "Design and analysis of dispersion engineered rib waveguides for on-chip mid-infrared supercontinuum," *J. Lightwave Technol.* **36**(10), 1993–1999 (2018).
- S. S. Bobba and A. Agrawal, "Ultra-broad mid-IR supercontinuum generation in single, Bi and tri layer graphene nano-plasmonic waveguides pumping at low input peak powers," *Sci. Rep.* **7**, 10192 (2017).
- T. S. Saini, T. H. Tuan, T. Suzuki, and Y. Ohishi, "Coherent mid-IR supercontinuum generation using tapered chalcogenide step-index optical fiber: Experiment and modelling," *Sci. Rep.* **10**, 2236 (2020).
- S. Yu, J. I. Lee, and A. K. Viswanath, "Time-resolved four-wave mixing signal in thick bulk GaAs," *J. Appl. Phys.* **86**, 3159 (1999).
- M. A. Foster, A. C. Turner, J. E. Sharping, B. S. Schmidt, M. Lipson, and A. L. Gaeta, "Broad-band optical parametric gain on a silicon photonic chip," *Nature* **441**, 960–963 (2006).
- S. Zlatanovic, J. S. Park, S. Moro, J. M. C. Boggio, I. B. Divliansky, N. Alic, S. Mookherjee, and S. Radic, "Mid-infrared wavelength conversion in silicon waveguides using ultracompact telecom-band-derived pump source," *Nat. Photonics* **4**, 561–564 (2010).
- H. Kuwatsuka, R. Akimoto, T. Ogasawara, S. Gozu, T. Mozume, T. Hasama, and H. Ishikawa, "Four-wave mixing in InGaAs/AlAsSb intersubband transition optical waveguides," *J. Appl. Phys.* **110**, 063114 (2011).
- R. L. Espinola, J. I. Dadap, R. M. Osgood, Jr., S. J. McNab, and Y. A. Vlasov, "C-band wavelength conversion in silicon photonic wire waveguides," *Opt. Express* **13**, 4341–4349 (2005).
- H. Fukuda, K. Yamada, T. Shoji, M. Takahashi, T. Tsuchizawa, T. Watanabe, J. Takahashi, and S. Itabashi, "Four-wave mixing in silicon wire waveguides," *Opt. Express* **13**, 4629–4637 (2005).
- T. Godin, Y. Combes, R. Ahmad, M. Rochette, T. Sylvestre, and J. M. Dudley, "Far-detuned mid-infrared frequency conversion via normal dispersion modulation instability in chalcogenide microwires," *Opt. Lett.* **39**, 1885–1888 (2014).
- T. S. Saini, T. H. Tuan, M. Matsumoto, G. Sakai, T. Suzuki, Y. Ohishi, "Mid-infrared wavelength conversion using dispersion engineered  $\text{As}_2\text{S}_5$  microstructured optical fiber pumped with ultrafast laser at 2  $\mu\text{m}$ ," *Opt. Lett.* **45**(10), 2736–2739 (2020).
- K. Nagasaka, H. T. Tong, H. P. T. Nguyen, T. Suzuki, and Y. Ohishi, "Far-detuned four-wave mixing for mid-infrared wavelength conversion in chalcogenide  $\text{As}_2\text{S}_5$  suspended core fiber," *Proc. SPIE* **10528**, 105281M (2018).
- K. Ikeda, R. E. Saperstein, N. Alic, and Y. Fainman, "Thermal and Kerr non-linear properties of plasma-deposited silicon nitride/silicon dioxide waveguides," *Opt. Express* **16**, 12987–12994 (2008).
- I. Agha, S. Ates, M. Davanço, and K. Srinivasan, "A chip-scale, telecommunications-band frequency conversion interface for quantum emitters," *Opt. Express* **21**(18), 21628–21638 (2013).
- A. S. Kowligy, D. D. Hickstein, A. Lind, D. R. Carlson, H. Timmers, N. Nader, D. L. Maser, D. Westly, K. Srinivasan, S. B. Papp, and S. A. Diddams,

“Tunable mid-infrared generation via wide-band four-wave mixing in silicon nitride waveguides,” *Opt. Lett.* **43**, 4220–4223 (2018).

- <sup>30</sup>A. G. Andreou, Z. K. Kalayjian, A. Apsel, P. O. Pouliquen, R. A. Athale, G. Simonis, and R. Reedy, “Silicon on sapphire CMOS for optoelectronic microsystems,” *IEEE Circuits Syst. Mag.* **1**(3), 22–30 (2001).
- <sup>31</sup>R. S. E. Shamy, H. Mossad, and M. A. Swillam, “Silicon-on-Sapphire (SOS) waveguide modal analysis for mid infrared applications,” *J. Phys. Commun.* **1**, 035011 (2017).
- <sup>32</sup>T.-J. Lu, B. Lienhard, K.-Y. Jeong, H. Moon, A. Iranmanesh, G. Grosso, and D. Englund, “Bright high-purity quantum emitters in aluminum nitride integrated photonics,” *ACS Photonics* **7**, 2650 (2020).
- <sup>33</sup>A. Jha, B. D. O. Richards, G. Jose, T. T. Fernandez, C. J. Hill, J. Lousteau, and P. Joshi, “Review on structural, thermal, optical and spectroscopic properties of tellurium oxide based glasses for fibre optic and waveguide applications,” *Int. Mater. Rev.* **57**(6), 357–382 (2012).
- <sup>34</sup>V. A. G. Rivera and D. Manzani, *Technological Advances in Tellurite Glasses: Properties, Processing, and Applications* (Springer, 2017).
- <sup>35</sup>S.-H. Kim, T. Yoko, and S. Sakka, “Linear and nonlinear optical properties of TeO<sub>2</sub> glass,” *J. Am. Ceram. Soc.* **76**(10), 2486–2490 (1993).
- <sup>36</sup>S. M. Pietralunga, M. Lanata, M. Feré, D. Piccinin, G. Cusmai, M. Torregiani, and M. Martinelli, “High-contrast waveguides in sputtered pure TeO<sub>2</sub> glass thin films,” *Opt. Express* **16**(26), 21662–21670 (2008).
- <sup>37</sup>S. J. Madden and K. T. Vu, “Very low loss reactively ion etched tellurium dioxide planar rib waveguides for linear and nonlinear optics,” *Opt. Express* **17**(20), 17645–17651 (2009).
- <sup>38</sup>H. C. Frankis, K. M. Kiani, D. Su, R. Mateman, A. Leinse, and J. D. B. Bradley, “High-Q tellurium-oxide coated silicon nitride microring resonators,” *Opt. Lett.* **44**(1), 118–121 (2019).
- <sup>39</sup>G. Ghosh, “Sellmeier coefficients and chromatic dispersions for some tellurite glasses,” *J. Am. Ceram. Soc.* **78**(10), 2828–2830 (1995).
- <sup>40</sup>M. J. Dodge, “Refractive index,” in *Handbook of Laser Science and Technology, Optical Materials: Part 2 Vol. IV* (CRC Press, Boca Raton, 1986), p. 30.
- <sup>41</sup>I. H. Malitson and M. J. Dodge, “Refractive index and birefringence of synthetic sapphire,” *J. Opt. Soc. Am.* **62**, 1405 (1972).
- <sup>42</sup>D. T. Spencer, J. F. Bauters, M. J. R. Heck, and J. E. Bowers, “Integrated waveguide coupled Si<sub>3</sub>N<sub>4</sub> resonators in the ultrahigh-Q regime,” *Optica* **1**(3), 153–157 (2014).
- <sup>43</sup>H. C. Frankis, K. M. Kiani, D. B. Bonneville, C. Zhang, S. Norris, R. Mateman, A. Leinse, N. D. Bassim, A. P. Knights, and J. D. B. Bradley, “Low-loss TeO<sub>2</sub>-coated Si<sub>3</sub>N<sub>4</sub> waveguides for application in photonic integrated circuits,” *Opt. Express* **27**(9), 12529 (2019).
- <sup>44</sup>T. S. Saini, T. H. Tuan, L. Xing, N. P. T. Hoa, T. Suzuki, and Y. Ohishi, “Coherent mid-infrared supercontinuum spectrum using a step-index tellurite fiber with all-normal dispersion,” *Appl. Phys. Express* **11**, 102501 (2018).
- <sup>45</sup>J. C. Travers, M. H. Frosz, and J. M. Dudley, “Nonlinear fibre optics overview,” in *Supercontinuum Generation in Optical Fibers*, edited by J. Dudley and T. Roy (Cambridge University Press, New York, 2010), Chap. 3, pp. 32–51.
- <sup>46</sup>Q. Li, L. Liu, Z. Jia, G. Qin, Y. Ohishi, and W. Qin, “Increased red frequency shift in coherent mid-infrared supercontinuum generation from tellurite microstructured fibers,” *J. Lightwave Technol.* **35**, 4740–4746 (2017).